High-Fidelity Experimental Simulations of Atmospheric Flow near Low-Intensity Fires in a Wildland-Urban Interface

Dongqi Lin[1*], Marwan Katurji[1], Peyman Zawar-Reza[1], Alena Malyarenko[1,2], Andres Valencia[3], Jiawei Zhang[4]

[1]Te Kura Aronukurangi / School of Earth and Environment, Te Whare Wānanga o Waitaha / University of Canterbury, Ōtautahi / Christchurch, Aotearoa / New Zealand
[2]Te Puna Pātiotio / Antarctic Research Centre, Te Herenga-Waka / Victoria University of Wellington, Aotearoa / New Zealand
[3]Te Tari Pūhanga Metarahi, Rawa Taiao / Department of Civil and Natural Resources Engineering, Te Whare Wānanga o Waitaha / University of Canterbury, Ōtautahi / Christchurch, Aotearoa / New Zealand
[4]New Zealand Forest Research Institute, Scion, Ōtautahi / Christchurch, Aotearoa / New Zealand

Key Points:

- High-resolution simulations reveal how forest canopy and urban structures modulate near-surface atmospheric flows near a low-intensity fire.
- Compared to flat terrain, the presence of vegetation and buildings introduces pulsed downwind heat transport.
- The wildland-urban interface facilitates further downwind transport of fire heat and more frequent pulsing than the wildland forest alone.

*Now at ARC Centre of Excellence for Climate Extremes, Monash University, Melbourne, Australia

Corresponding author: Dongqi Lin, dongqi.lin@monash.edu

Abstract

With increased urbanization, fires in the wildland urban interface (WUI) have become a severe problem worldwide. The unique features of WUI may influence the atmospheric flows in the vicinity of fire. This study utilizes the parallelized large eddy simulation model (PALM) system for fire-atmosphere simulations of Bottle Lake Forest, Christchurch, New Zealand. Over 3000 residential buildings are situated around the 7 km^2 forest, with many homes only 50 m away from the forest edge. We conducted high-fidelity fire-atmosphere simulations with the finest grid spacing of 4 m. Wildland forest (WF) and flat terrain simulations were conducted to provide a reference for comparison with WUI simulations. Fire-weather conditions for the 2022/2023 New Zealand fire season were selected based on the Fire Weather Index (FWI). Data from previous fire field campaigns were obtained to represent a low-intensity fire heat forcing. The results reveal a pulsing behavior in downwind heat transport when the forest canopy is included. Furthermore, the presence of the WUI is associated with extended downwind fire heat transport compared to WF and flat terrain scenarios. This study is the first to simulate atmospheric flows near fires in a WUI setting with such high fidelity. The findings highlight the critical role of WUI features in shaping fire-atmosphere dynamics, though further research is required to disentangle the contributions of individual WUI components to these effects.

Plain Language Summary

As cities expand, fires in areas where wildlands and urban developments meet — called the wildland-urban interface (WUI) — are becoming a growing challenge worldwide. These fires are influenced by the unique features of WUI environments, which can affect how heat and smoke travel through the atmosphere. In this study, we used very high resolution simulations to explore the atmospheric flows near fires under the influences of the Bottle Lake Forest WUI in Christchurch, New Zealand, where a forest fire could threaten nearby homes. The simulations showed that the presence of forest causes a pulsing effect in heat transport downwind of the fire. Additionally, the WUI enabled fire heat to travel further along the wind, compared to scenarios without urban development. Our WUI fire simulations demonstrate high fidelity, which has not been previously achieved in other studies. The findings highlight how urban developments near forests can alter flow patterns near the fire and emphasize the need for further research to support better fire management and urban planning.

1 Introduction

The intensity and impacts of wildfires have been growing across the world. Human settlements have suffered significantly due to wildfires, especially in the wildland-urban interface (WUI) (A. Sullivan et al., 2022). The WUI is usually defined as the area where human development, such as houses, comes into close contact with natural, undeveloped areas dominated by wildland vegetation (Radeloff et al., 2005). The WUI fire problem is usually two-fold, encompassing climate and human activities. Climate is the primary driver of fire activity (Andela et al., 2017). Many studies have found that natural processes are linked to increased wildfire intensity, such as a decrease in fire season precipitation (Holden et al., 2018), and an increase in temperatures (e.g., Gutierrez et al., 2021; Mueller et al., 2020). A drier and warmer climate could lead to longer, hotter, and drier fire seasons, coinciding with more intense fire events and higher mortality. The secondary driver is human activities associated with land-use changes. The expansion of human settlements changes the landscape of the natural wildland. The road development allows easier access to combustible fuels, and the expansion of electrical transmission lines adds more fire risks to the WUI (Chen et al., 2024). Therefore, the WUI fire problem and its high social and economic costs have become a rising threat.

Similar to countries like the United States, Canada, and Australia, New Zealand witnessed a considerable increase in the total WUI area (Chen et al., 2024). Although New Zealand has a population of only 5 million people and covers a land area of approximately 268,021 km^2, it has experienced a great number of wildfires in recent years. For the year between 1 July 2020 and 27 June 2021, 4,586 fires occurred, with 13,348 hectares burnt (Fire Emergency New Zealand, 2021). Wildfires in New Zealand were relatively rare before the establishment of human settlement in the late 13th century (Perry et al., 2014). Although most of the fires in New Zealand are small (averaging less than 1 hectare; Pearce, 2018), a few large devastating wildfires have occurred during the past few years. In 2017, the Port Hills wildfire burned 1,660 hectares, forced over 1400 residents to evacuate, destroyed 9 homes, and cost millions to suppress, plus much more paid out by the insurers (Pearce, 2018, and citations therein). In 2020, the Lake Ōhau fire burned approximately 5043 hectares and destroyed 48 homes and buildings (Fire Emergency New Zealand, 2022). In 2024, close to the location of the 2017 wildfire, another fire occurred in the Port Hills, causing thousands of people to leave their homes. The exact damage and cause of the 2024 Port Hills Fire are still under investigation.

Among the many WUIs in New Zealand, in this study, we focus on the WUI of Bottle Lake Forest (BLF), Christchurch, New Zealand. Since Christchurch is the largest city in the South Island of New Zealand, there is a rising concern around its WUI fire problem. Figure 1 shows the location and landscape of the BLF WUI. The BLF area contains a pine forest of over 7 km^2 surrounded by more than 3000 residential buildings. The pine forest height is around 22-30 m. Many buildings are within 100 m of the forest precinct, which could be under serious fire danger in case of a forest fire in the area.

In this paper, we investigate how the presence of the BLF WUI influences the atmospheric response to a temporally invariant heat source at the ground, which resembles a low-intensity fire. The atmospheric and fire processes are multiscale and nonlinear, making fire-atmospheric interactions complex. The atmospheric processes can impact fire from the microscale (sub-meter to kilometer) to the mesoscale (10 to 200 km), while fire modifies the atmospheric flows with its strong forcing of heat (e.g., Dickinson et al., 2021; Finney et al., 2015; A. L. Sullivan, 2017; Zhang et al., 2023). To understand fire-atmosphere interactions, the scientific community has developed a range of models, from traditional empirical approaches to modern models that couple fire behavior with computational fluid dynamics (CFD) or numerical weather prediction (NWP) models (A. L. Sullivan, 2009a, 2009b; Bakhshaii & Johnson, 2019). While many sophisticated coupled models exist (e.g., Linn et al., 2002; Mell et al., 2007; J. Coen, 2013; J. L. Coen et al., 2013; Dahl et al., 2015; Filippi et al., 2013), no former studies have examined the impact of WUI on atmospheric flows near fires using a high-resolution turbulence-resolving model. As the WUI land surface imposes a complex forcing of heat and momentum on the Atmospheric Boundary Layer (ABL), we require a model capable of resolving turbulent atmospheric flows within a high-fidelity WUI landscape.

Therefore, we use the Parallelized Large Eddy Simulation (LES) Model (PALM; Maronga et al., 2015, 2020). PALM can conduct very fine grid spacing simulations (e.g., 4 m in this study) with detailed urban surface (Resler et al., 2017) and plant canopy modules (Maronga et al., 2020), allowing an explicit representation of the buildings and forest that constitute the WUI. While PALM has been used for fire–atmosphere turbulent energy transport (Zhang et al., 2023) and firebrand transport (Dal-Ri dos Santos & Yaghoobian, 2023), its application to study the impact of a realistic WUI on fire-induced flows is novel. For representing fire heat, we adopt the "hot plate" method, using a static surface heat source. Similar to previous hot plate studies (e.g., Kiefer et al., 2024; Zhang et al., 2023; Kiefer et al., 2018, 2016, 2015), we use a one-way fire–atmosphere model. In one-way models, the fire modifies the simulated wind field, but the feedback from atmospheric perturbations on the fire itself is not accounted for (Kiefer et al., 2024).

Figure 1. Maps and images depicting the location and landscape of the Bottle Lake Forest (BLF) area in Christchurch, New Zealand. Bottom left: Maps of New Zealand and Christchurch (©MapTiler and ©OpenStreetMap). Top left: Satellite imagery of the BLF area (©Google Earth). The yellow pin indicates the location of a SoDAR (Sonic Detection And Ranging) operated between November 2022 and April 2023. The blue pin marks the location of the automatic weather station (AWS) operated by Fire Emergency New Zealand (FENZ). Top right: zoomed-in image of the WUI. For the scale reference, the approximate length of 100 m is shown between the edge of the forest and the residential area. Bottom right: a 3D map of the landscape in the BLF WUI rendered on top of the satellite imagery. High topography is colored in orange, the forests are colored in green, and the buildings are plotted as white 3D blocks. Map data contain Christchurch 1 m digital surface data (Envirionment Canterbury Regional Council, 2020).

We conducted three sets of simulations with realistic BLF WUI, forest-only wildland, and flat terrain, to compare the influence of different landscape components. The results show that while the forest canopy itself induces a pulsing behavior in downwind fire heat transport, the inclusion of buildings acts to amplify these pulses. We further conducted zero-crossing and wavelet analysis to quantify how the characteristics of these heat pulses (e.g., frequency and amplitude) differ across the three simulation cases. These quantitative analyses allow us to identify the contribution of both the forest canopy and the buildings to the overall dynamics of heat transport.

We begin the rest of the paper by describing the model and the design of the experimental case study (Section 2). We then examine the simulation results of fire heat transport and the flow characteristics (Section 3). Finally, we present discussions and conclusions in Sections 4.

2 Model configuration and experiment design

2.1 PALM domain configuration

PALM version 22.10 is used in this study. PALM solves the turbulent flow based on the non-hydrostatic incompressible Navier-Stokes equations under the Boussinesq approximation (Maronga et al., 2015). The assumption of incompressibility is appropriate for fire-atmosphere simulations (Tang, 2017; Zhang et al., 2023). The turbulence closure is based on a modified three-dimensional Deardorff 1.5-order scheme, assuming a proportional relationship between the energy transport by sub-grid-scale eddies and the local gradient of the average quantities (Deardorff, 1980; Maronga et al., 2015).

The domain configuration of simulations conducted in this study is shown in Table 1 and Figure 2. The datasets and tools used to produce the PALM static geospatial information input are identical to those described in Lin et al. (2024). The first domain (D01) has flat terrain only with periodic boundary conditions and a homogeneous land use type of grassland. Christchurch is mainly surrounded by grassland. The flat terrain domain is designed to generate realistic inflow turbulence, and to transfer synoptic forcing to the child domains while preventing numerical instability stemming from steep terrain near the lateral boundaries (Lin et al., 2023). This configuration resembles the turbulence recycling method, where upstream flat terrain generates turbulence as inflow for downstream domains. Unlike the traditional turbulence recycling approach in PALM, which restricts inflow to one domain side, our method removes this limitation, allowing a north-westerly flow described below. Regarding the nested domains, the second domain (D02) only includes topography with land use information derived from the New Zealand Land Cover Database (LCDB) V5.0 (Landcare Research, 2020). In addition to topography and land use information, the third and fourth domains (D03 and D04) include information on pavements and streets, buildings, and plant canopy. The simulations use one-way domain nesting, with all child domains having open boundaries. Realistic inflow turbulence and synoptic forcing are passed from D01 to the child domains, but processes in the child domains do not influence their parent domain.

The land surface model (Gehrke et al., 2021) and the radiation model (Maronga et al., 2020) were switched on in all domains. The time step of the radiation model in PALM was set to 360 seconds. The radiative transfer model (Krč et al., 2021) was switched on for D03 and D04, where forest and urban canopies are present. In the radiation model, hourly long-wave and short-wave radiation fields from WRF simulations were used to provide a more realistic representation of radiative forcing. The WRF simulations, configured similarly to those described in Lin et al. (2021), were conducted and are hosted by the New Zealand Modeling Consortium (envlib.org; last accessed: 14 July 2025). Only D03 and D04 include plant canopy models (Maronga et al., 2020) and/or the urban surface (Resler et al., 2017). The landscape of D04 is shown in Figure 2b. The terrain in D04 is predominantly flat, with

slight variations in elevation. The forest area in D04 can be identified by a high leaf area index (LAI>2.5 m^2 m^{-2}). The averaged vertical profile of leaf area density (LAD) of the fire location is shown in Figure S1. We focus on D04 for analysis and discussions.

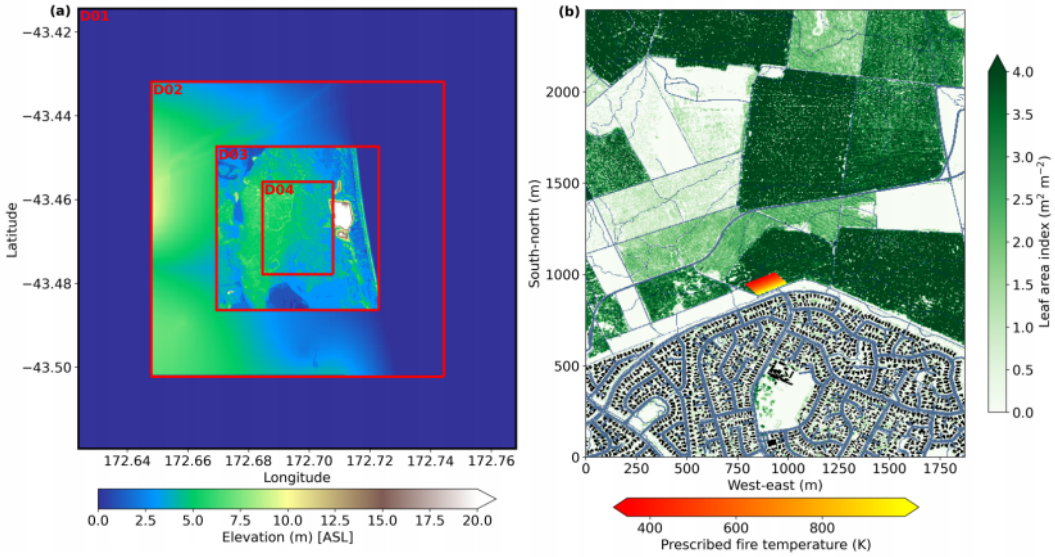

Figure 2. (a) A topographic map (elevation above sea level) showing the PALM simulation domain configuration. The simulation includes four nested domains (D01, D02, D03, and D04). D01 is a flat terrain domain. (b) Land use information of D04: the forest is marked by leaf area index (LAI) in green, buildings are shown in black, and pavements and streets are colored in light blue. The red patch marks the location of the prescribed temperature, representing fire.

2.2 Fire weather case selection

To reproduce fire weather, we examined the fire weather index (FWI) during the 2022/2023 New Zealand fire season. We calculated FWI using data obtained from an automatic weather station (AWS) located in the BLF area operated by Fire Emergency New Zealand (FENZ) (location see blue pin in Figure 1). The FWI calculation is identical to the vector wind change FWI described by Brody-Heine et al. (2023). The AWS datasets are freely accessible via the New Zealand Modeling Consortium (envlib.org; last accessed: 14 July 2025). The 5th of February, 2023, was identified as a high FWI day. The FWI was around 24.3, which is the second highest between December 2022 and May 2023. This number is above the threshold of 20, which represents a very high and extreme fire danger potential (see long-term analysis by Brody-Heine et al., 2023, and citations there in). We use this value solely as an indicator of fire danger potential, while a full validation of this threshold against local fire occurrence data across New Zealand is a separate undertaking and beyond the scope of this simulation study.

The high FWI on 5th February 2023 coincides with a foehn event picking up in the late afternoon, bringing strong and dry north-westerlies over Christchurch. A foehn event in New Zealand occurs when moist air is forced over the windward side of the mountain ranges, such as the Southern Alps, leading to rapid increases in wind speed and temperature in the leeward side of the ranges (refer to e.g., Sturman & Tapper, 2006). A SoDAR (Sonic Detection And Ranging; location see yellow pin in Figure 1) was operating inside the BLF area between November 2022 and April 2023. It recorded a wind speed of approximately 4.4 m s^{-1} near the forest canopy top (approximately 30 m above ground level) and 25 m s^{-1}

Table 1. PALM domain configuration for WUI, wildland forest only (WF), and flat terrain (Flat) simulations.

Domain	**D01**	**D02**	**D03**	**D04**
Number of grid points (x, y, z)	324*324*192	216*216*144	360*360*360	468*612*648
Domain size (x, y, z)	11664 m *11664 m*6912 m	7776 m*7776 m*5184 m	4320 m*4320 m*4320 m	1872 m*2448 m*2592 m
Horizontal grid spacing(dx, dy)	36 m	36 m	12 m	4 m
Vertical grid spacing (dz)	36 m	36 m	12 m	4 m
Land use (WUI)	Flat terrain with grassland only	Full terrain with realistic land use categories	Full terrain with realistic land use categories, forest canopy and urban canopy	Full terrain with realistic land use categories, forest canopy and urban canopy
Land use (WF)	Flat terrain with grassland only	Full terrain with realistic land use categories	Full terrain with realistic land use categories, and forest canopy. All urban features removed.	Full terrain with realistic land use categories, and forest canopy. All urban features removed.
Land use (Flat)	Flat terrain with grassland only	Flat terrain with grassland only	Flat terrain with grassland only	Flat terrain with grassland only

at around 300 m above ground level. With such weather conditions, fire is likely to occur, spreading from the forest into the residential area in the south.

Figure 3 shows the vertical profiles used to initialize the simulations. These profiles were obtained from the SoDAR (up to 450 m) and WRF simulations (above 450 m) and were used for initialization only, with no offline nesting enabled between WRF and PALM. All PALM simulations started at 0700 UTC on 5th February 2023 (equivalent to 1900 local standard time), and the simulation time is 2.5 hours. The fire was switched on for the last 30 minutes of the simulation. The first hour of the simulations is considered model spin-up. We chose the simulation timing to reflect a period when northwesterly winds were strongest and most persistent (not shown), consistent with the observed foehn-driven fire weather conditions.

To understand the influences of the WUI on the fire-atmospheric flows, we conducted three sets of simulations. One has the full WUI environment, one has the wildland forest only (hereafter WF), and the last one has flat terrain (hereafter Flat) with land use configured as grassland only for all nested domains. For each set of the simulations, a baseline simulation with no fire throughout the entire simulation was conducted along with a simulation with fire switched on after 2 hours into the simulation. Hereafter, we denote these simulations as WUI_Fire (WUI environment with fire switched on), WUI_Base (WUI environment with no fire), WF_Fire (WF environment with fire switched on), WF_Base (WF environment with no fire) Flat_Fire (flat terrain with fire switched on), and Flat_Base (flat terrain with no fire).

2.3 Fire heat representation

The fire fields prescribed in the simulations were derived from an infrared overhead video acquired during an instrumented prescribed burn experiment in Rakaia Gorge, Canterbury, New Zealand. The overstory canopy primarily consisted of gorse. An unmanned Aerial Vehicle (UAV) was used to acquire the footage, and the resulting temperature profile was compared with 25 in-situ temperature probes evenly spaced inside the experimental plot. For more details, readers are referred to Katurji et al. (2022); Valencia, Melnik, Kelly, et al. (2023); Valencia, Melnik, Sanders, et al. (2023). To derive a normalized temperature curve (hereafter the fire curve), 20,000 data points of brightness temperatures were analyzed from the infrared footage. Only measurements exceeding fireline intensities of 1000 kW m^{-2} were included to minimize errors related to footage stabilization and flame visualization. All measurements of brightness temperatures were adjusted to 100 °C for consistency. The fire curve describing the fire temperature T_{fire} varying over the distance (x) takes the form of

$$T_{fire}(x) = 1.035\frac{b}{a} * \exp\left(-\frac{x-c}{b} - \exp\left(-\frac{x-d}{e}\right)\right) * T_{peak} \qquad [K] \tag{1}$$

where a, b, c, d, and e are least-square fitting coefficients. Their values are -0.135, -0.632, 1.782, 0.925, -0.036, respectively. T_{peak} represents the highest temperature of fire. This is an empirical curve similar to the firebrand accumulation temperature curve described by Cantor et al. (2023).

Since we do not have the exact temperature curve for the pine forest, we obtained the normalized fire curve and prescribed the highest temperature of 993 K. The temperature of 993 K was selected based on the oak wood and pine wood fire brand temperature described in Dal-Ri dos Santos and Yaghoobian (2023); Matvienko et al. (2022); Tse and Fernandez-Pello (1998). The temperature curve shown in Figure 3d represents the temperature characteristics of fire (preheating, combustion, and smoldering). However, note that, in this study, we only prescribed part of the fire curve (gray box in Figure 3d) as a representation of fire heat forcing only. This temperature field was prescribed from the surface

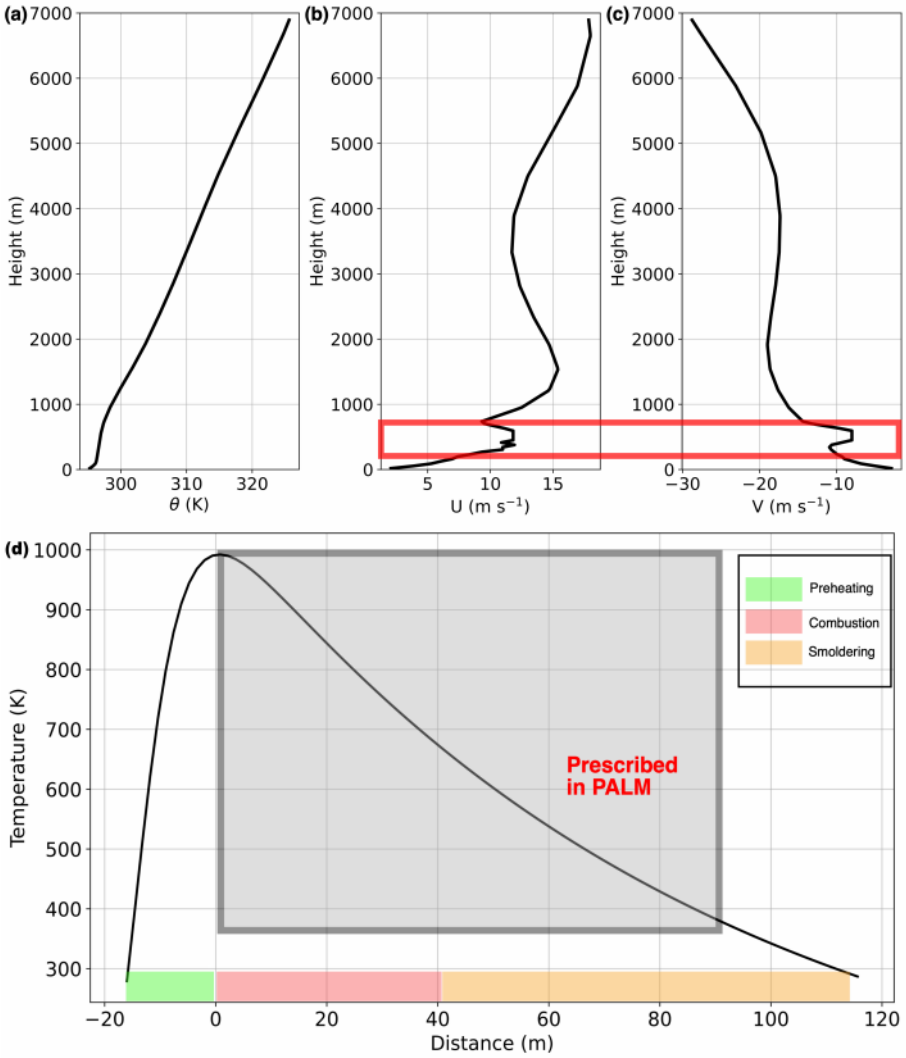

Figure 3. Vertical profiles of (a) potential temperature (θ), (b) u-component of wind, and (c) v-component of wind for simulation initialization. The red box marks the height of a strong wind shear observed by the SoDAR. Panel (d) shows the fire temperature curve prescribed in the PALM simulations. The grey box indicates the temperature profile prescribed in the simulations to represent fire. The three characteristics of the fire temperature curve are marked in green (preheating), red (combustion), and yellow (smoldering).

to the height of the forest canopy. The simulated fire sensible heat flux is approximately 14 kW m^{-2} near the fire front, aligning with the range of 1-minute mean sensible heat fluxes of low-intensity fires (8–155 kW m^{-2}) described in previous studies (e.g., Clements et al., 2007; Heilman et al., 2015; Kiefer et al., 2018; Heilman et al., 2021, and citations therein). Similar to Zhang et al. (2023), the location of the prescribed heat forcing is static, and no initiation/combustion processes are discussed in this study. The implementation of the fire curve in the simulations is illustrated as the red patch in Figure 2b.

3 Results

In this section, we compare the results between the WUI simulations, the WF simulations, and the Flat simulations. Here, we mainly focus on the 30-minute period after the fire was switched on. Hereafter, the time within the simulations is reported in HH:MM:SS format relative to the start time, with "00:00:00" corresponding to the model initialization time (0700 UTC on 5th February 2023), denoted in hours, minutes, and seconds, e.g., "01:40:50" for 1 hour 40 minutes and 50 seconds into the simulation (0840 UTC + 50 s).

We first describe the overall behavior of fire-induced flows (Section 3.1) and summarize the fire heat transport footprints (Section 3.2). We then present the general statistics based on the land use categories (Section 3.3), the spatial averaged time series (Section 3.4), and zero-crossing analysis (Section 3.5) to quantify the characteristics of downwind fire heat transport. Finally, we adopted wavelet analysis with no-averaged time series to further reveal the detailed time-dependent structure of the heat pulses (Section 3.6).

3.1 Fire in the WUI

Figure 4 shows one-minute averaged horizontal cross-sections of potential temperature (θ), and wind components (u, v, and w) at 14 m above the surface at 02:13:00. In this paper, u and v denote the horizontal wind components in the cardinal directions, representing the west–east and the south–north winds, respectively. Note that the model output is every second, and the second hour of the simulation (02:00:00) corresponds to the local sunset time. The prescribed heat source induces strong convergence and vertical motion in all cases. Near the fire front, u is strongly negative to the east and positive to the west, while v shows a similar dipole pattern with southerly flow ahead of the fire and northerly flow behind it. Vertical velocity (w) is characterized by updrafts at the fire front and flanking downdrafts on both sides.

While the general flow structure is consistent, the presence of forest and buildings substantially alters the patterns. In WUI_Fire and WF_Fire, vegetation outlines are clearly visible as zones of reduced wind speeds, especially in dense forest regions (LAI>3.5 m^2 m^{-2} in Figure 2b). The urban area in WUI_Fire exhibits higher θ, reflecting reduced surface cooling and enhanced heat retention due to urban materials. In contrast, Flat_Fire shows the highest overall θ, as low surface roughness facilitates near-surface mixing and suppresses radiative cooling after sunset.

Flat_Fire also presents a more symmetric and organized structure in the downwind transport of heat and flow, with vertical motion (w) nearly symmetric about the fire centerline (dashed red line in Figure 4a). In contrast, WF_Fire and WUI_Fire show broader, more asymmetric inflow and wake regions, with stronger easterly and southerly components extending farther from the fire (Figure 4). These differences illustrate how surface heterogeneity modulates the wind patterns downwind of the fire with a scale of a few hundred meters.

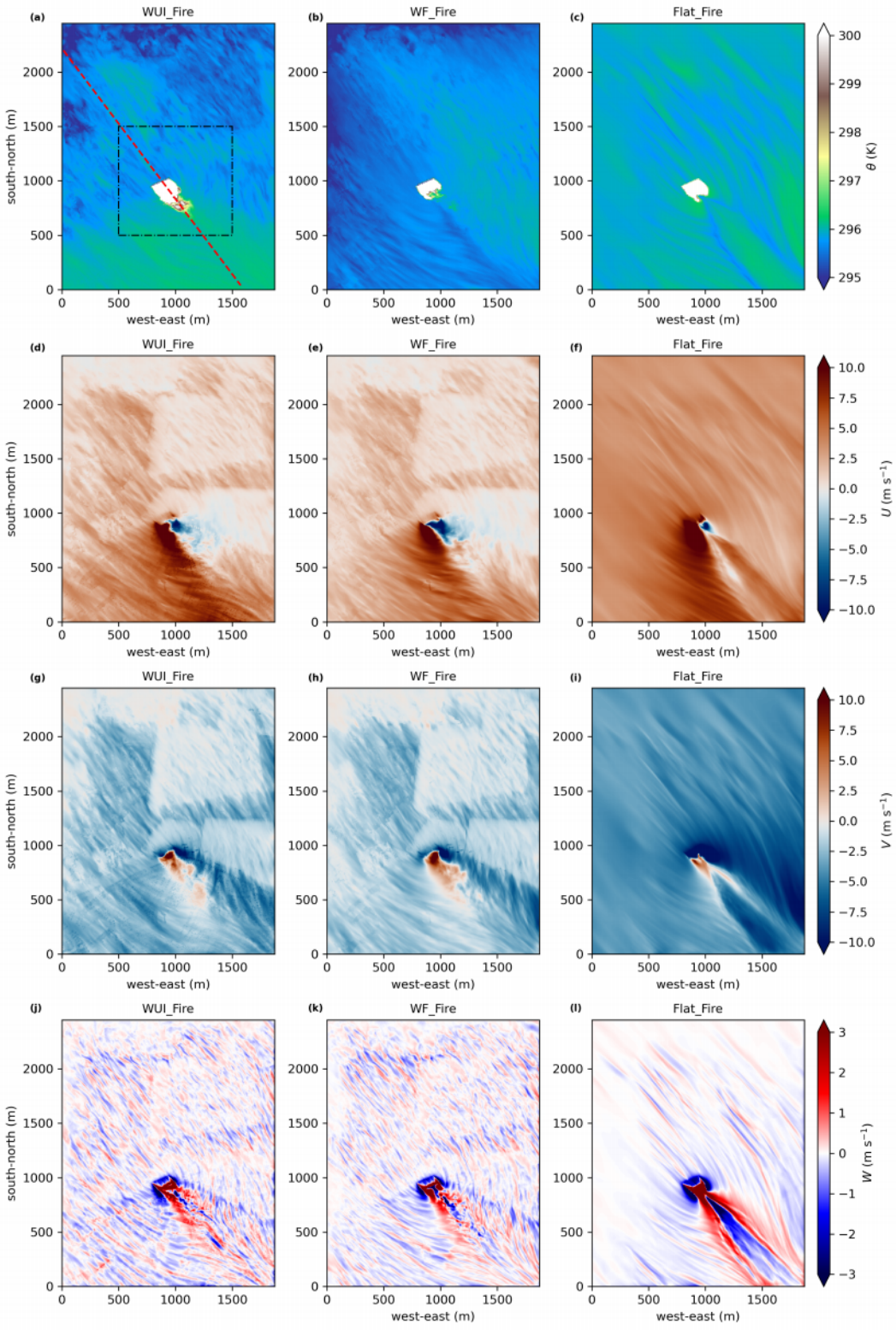

Figure 4. One-minute averages at 02:13:00 showing horizontal cross sections of θ (a-c), u (d-f), v (g-i), and w (j-l) at 14 m above the surface. From left to right, the first column is for WUI_Fire, the second column for WF_Fire, and the third column for Flat_Fire. In panel (a), the dashed red line indicates the location of vertical cross sections shown in Figure 5g-i. The dashed black box marks the area shown in Figure 5a-f.

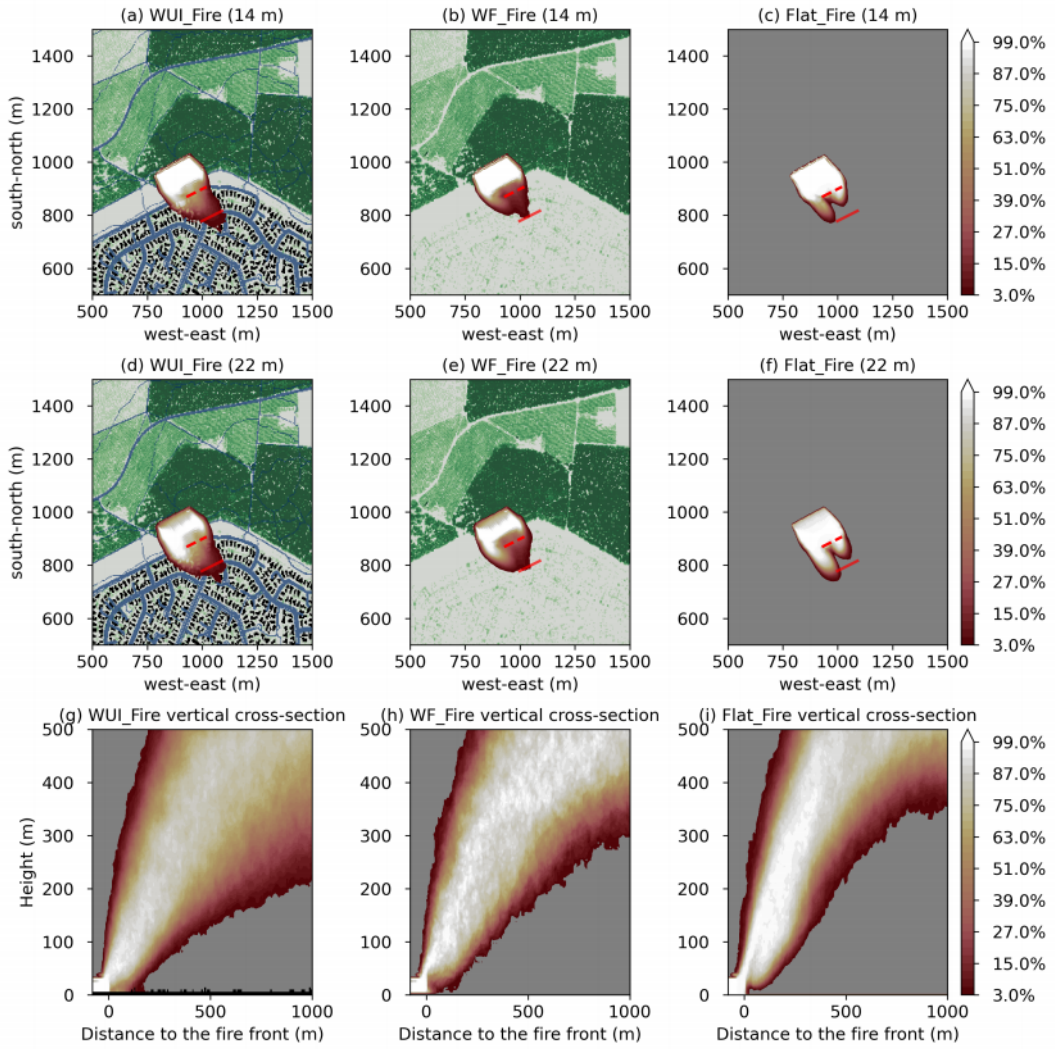

Figure 5. Percentage of occurrence when temperature increase of 1 K is captured at each grid point, comparing fire simulations to their baseline counterparts. Panels (a-c) are for 14 m above the surface, panels (d-f) are for the forest canopy height (22 m), and panels (g-i) are for the vertical cross-sections shown in Figure 4. From left to right, the columns are for the WUI simulations, the WF simulations, and the Flat simulations, respectively. The WUI landscape of Figure 2b is shown in (a) and (d). Only the forest landscape is shown for WF (b and e). Refer to Figures 4a for locations of (a)-(f). The dashed and solid red lines in (a)-(d) indicate the location of Willoughby Lane (WLN) and Anglesea Avenue (AAV), respectively. The distance between the two streets is approximately 95 m.

3.2 Fire footprints

Upon examining the temporal evolution of the simulations, we noticed that WUI_Fire presents a heat pulsing behavior with the downwind transport of heat fluctuating between the fire front and approximately 150 m downwind. This pulsing behavior is less noticeable in WF_Fire and nearly absent in Flat_Fire. The vertical cross-sections of θ and w along the fire present the same pulsing behavior near the surface (not shown). Readers are referred to the supplements for animations showing instantaneous snapshots of the simulations.

Due to the turbulent nature of LES, different results could be produced at every single time step. Instantaneous snapshots do not conclude the general feature of the simulations. Therefore, we present Figure 5 to summarize the downwind impact of fire. Figure 5 shows the percentage of time that a grid point sees an increase in θ of more than 1 K after the fire is switched on. A threshold of 1 K was chosen to highlight the farthest downwind heat transport. Higher thresholds (e.g., 5 K and 10 K) yield similar results (not shown). The temperature difference was calculated by subtracting a fire simulation from its baseline counterpart. The total time of the fire is 1800 seconds, and one-second output is used in this analysis, allowing sufficient data points for this kind of analysis. This analysis gives us an overview of the heat footprints, showing the potential downwind impact of fire heat. The footprints were calculated at two heights: 14 m above the surface (mid forest canopy level) and 22 m above the surface (near the forest canopy top). We picked the two streets in front of the fire to reference the distance and the impact of the downwind heat. Willoughby Lane (WLN) is approximately 45 m in front of the prescribed fire, and down to the south-east of WLN is Anglesea Avenue (AAV). AAV is about 95 m away from WLN. The locations of WLN and AAV are marked by dashed and solid red lines in Figures 5a-f, respectively.

In general, the heat footprints are more spatially confined near the location of the prescribed fire in Flat_Fire, occupying a smaller, more defined area in both the horizontal and vertical directions (Figure 5c, f, and i). Figures 5c and 5f show that almost no heat is transported to AAV near the surface, and little heat reached over AAV at the forest canopy top. The shape of Flat_Fire footprints shows a dual-peak structure at both 14 m and 22 m above the surface, with a longer distance of downwind heat transport near the west and east sides of the fire and a shorter distance near the center line. The symmetrical footprints in Flat_Fire (Figure 5c and 5f) resemble the symmetrical patterns in w as shown in Figure 4l. In WUI_Fire, the downwind heat reaches AAV at both 14 m and 22 m above the surface (Figures 5a and 5d). The density of the footprints decreases with distance ahead of the fire, encompassing high values of 75% close to the center line of the fire patch near WLN at the mid forest canopy (14 m). Although the footprints in WF_Fire (Figures 5b and 5e) resemble those in WUI_Fire, the downwind heat transport in WF_Fire rarely goes beyond AAV (Figure 5b and 5e). At 14 m, the footprints in WUI_Fire and WF_Fire (Figure 5a-b) do not show a dual-peak pattern as in Flat_Fire (Figure 5c and5f). The dual-peak pattern, however, is noticeable at the canopy height in WUI_Fire and WF_Fire for values greater than 87% (Figure 5d). We consider the presence of the dual-peak footprints as an indication that the impacts of the WUI and WF surfaces decrease with height.

Despite such a decrease, the impact of the WUI and WF on the atmospheric flows does not simply diminish above the forest canopy height. As shown in Figure 5g-h, the heat plumes travel much further downwind at all heights following the order of WUI_Fire (extended to 900 m downwind at 200 m high), WF_Fire (extended to 600 m downwind at 200 m high), and Flat_Fire (extended to 400 m downwind at 200 m high). Some of the plume-affected areas have an occurrence rate of more than 63%, equivalent to 19 minutes. The vertical footprints of the heat plume bend more towards the surface following the order of WUI_Fire, WF_Fire, and Flat_Fire (Figure 5g-i). In Flat_Fire, most of the heat goes upwards due to buoyancy, transporting little heat toward the surface and downwind. In WF_Fire, the vertical footprint tilts more towards the surface compared to Flat_Fire, suggesting the atmospheric flow exiting the forest may introduce downdrafts at the forest edge. The tilting of the vertical footprints is much more notable in WUI_Fire. The vertical

footprints in WUI_Fire (Figure 5g) reach the surface within 100 m ahead of the fire front with an occurrence rate above 10% (equivalent to 3 minutes). Such impact of heat reaching the surface over 50 m downwind is absent in both WF_Fire and Flat_Fire. These results suggest that the WF and WUI modify the atmospheric flows near the fire and, subsequently, the downwind transport of heat from the fire. The wildland forest has strong influences on the atmospheric flow, but the inclusion of urban surfaces strengthens the heat transport onto the surface and further downwind of fire.

3.3 Land use-based statistical distributions

To examine the WUI flow characteristics in more detail, violin plots of u, v, w, and total turbulence kinetic energy (TKE) at 14 m above the surface are shown in Figure 6. The results are similar at the forest canopy height (22 m; Figure S3), except that the magnitudes of all variables are slightly greater. These violin plots compare the last 30 minutes of baseline simulations and fire simulations to show the influences of land use on the atmospheric flows and the impact of fire.

Based on the dominant land use (Landcare Research, 2020), D04 was classified into three parts: forest, interface, and urban. The details of the land use classification are shown in Figure S2. The northern part of D04 is covered by wildland forest, the southern part consists of residential areas with urban developments, and the grassland between the forest and urban areas is considered the interface. Note that these classifications serve solely as location references. The WUI refers to the combined environment of forested areas, urban regions, and their interface zones. Data for the entire simulation domain (denoted as All) are also presented in Figure 6 as a reference for the overall features of the simulations. Note that the forest area has more data points than the interface and urban area. Urban land accounts for 29.9% of D04, with buildings covering 24.3% of that urban area and 7.3% of the entire domain. The violin plots are scaled such that the widest part is the maximum data density.

All subplots in Figure 6 show an increase in the variable magnitudes when the fire is switched on. The impact of the fire is the least significant over the forest area in all simulations at both heights. The forest area is located upwind the prescribed heat source and hence experiences the least disturbances. Looking at 14 m above the surface, the amplification in u is the strongest in the interface, followed by the urban area in all simulations (Figure 6a, e, i). In WUI_Base, u in the interface presents a higher median value, indicating an acceleration of the flow entering this area where the friction is lower (Figure 6a). This is similar in WF_Base. In Flat_Base, the difference in u is subtle across the areas, since the surface roughness is uniform throughout the domain. The variations in the violin plots reflect only the data extraction locations (Figure 6i). In Flat_Fire, u has a high distribution where u >8 m s^{-1}. This is absent in WUI_Fire and WF_Fire. The figures of v show analogous patterns to u. The interface in the WUI simulations coincides with the most significant intensification of v wind velocity in both WUI_Base and WUI_Fire (Figure 6b). This is similar in WF_Base and WF_Fire, while the differences between the interface and the urban areas are less pronounced (Figure 6f). In Flat_Fire, one can notice a secondary peak in v distribution where v <-6 m s^{-1} (Figure 6j). This high density signal is absent in WUI_Fire and WF_Fire.

The violin plots of w show that the flow entering the interface and the urban areas coincide with amplified vertical motions of the flow in both WUI_Fire and WF_Fire(Figure 6c, g), which is absent in Flat_Base (Figure 6k). Nevertheless, in the fire simulations, the impacts of WUI and WF are less pronounced in w. The violin plots of w for WF_Fire resemble those for WUI_Fire. This may be because of the fact that violin plots only capture the bulk characteristics of the flow. More characteristics of w are discussed in the sections below. In Figures 6d, 6h, and 6i, the fire simulations present a notable intensification of TKE compared to their baseline counterparts. This is expected due to the extra heat forcing

introduced into the fire simulations. WUI_Base and WF_Base show similar patterns of TKE with the lowest TKE over the forest area, followed by the interface, and then the urban area (Figure 6d, h). The TKE in WUI_Base over the latter two areas is higher than that in WF_Base, due to the presence of the urban interface. In the Flat simulations, the increase in TKE with fire is strongest in the interface, followed by that in the urban (Figure 6l). The TKE magnitude is higher in the WF simulations compared to their Flat counterparts. Furthermore, the TKE is even greater in the WUI simulations than in the WF simulations. This supports our hypothesis that, while WF influences atmospheric flows, WUI introduces additional modifications. Subsequently, the downwind heat transfer is able to reach further away from the fire.

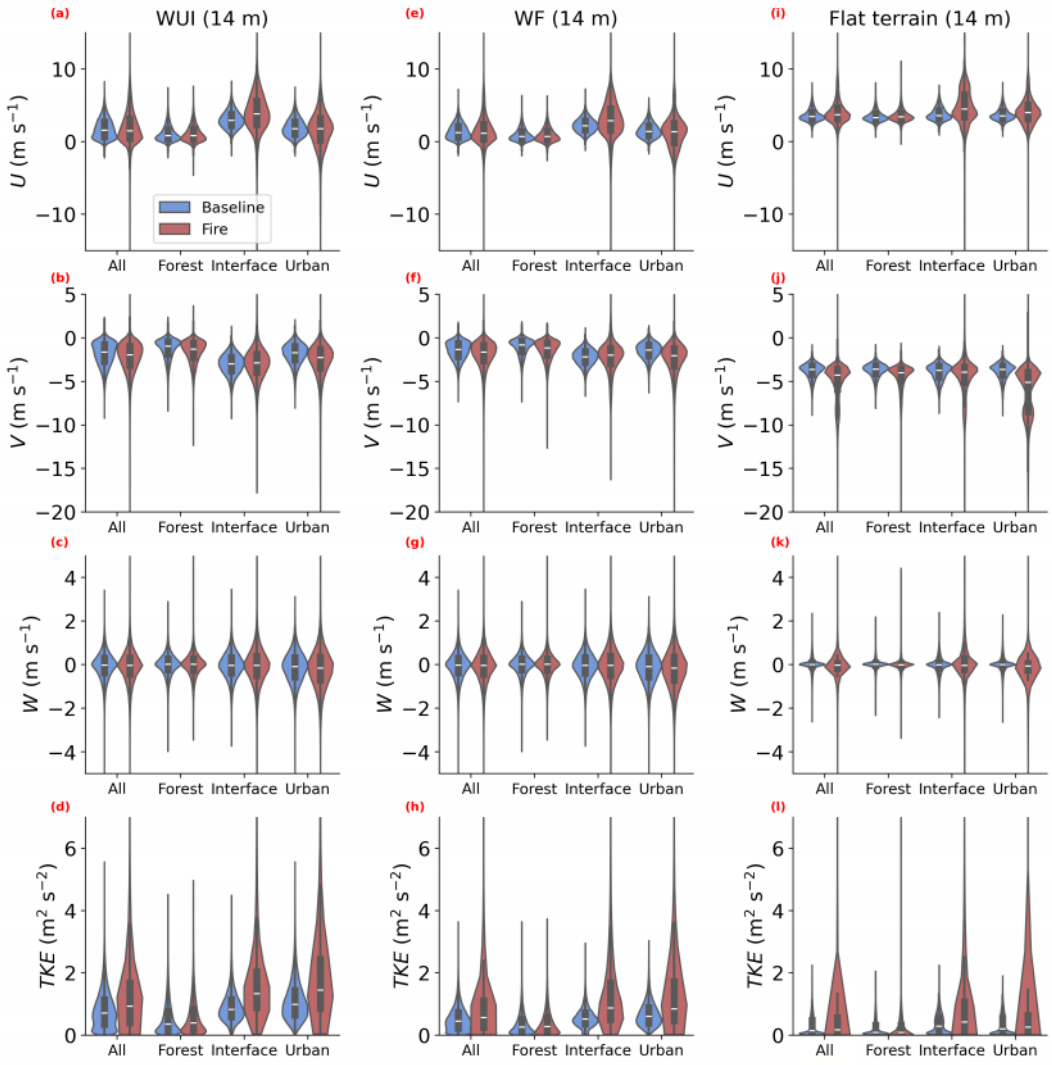

Figure 6. Violin plots comparing u (a, e, and i), v (b, f, and j), w (c, g, and k), and TKE (d, h, and l) at 14 m above the surface for the forest, interface, and urban areas between baseline simulations (blue) and their fire counterparts (red). From left to right, the columns are for WUI simulations, WF simulations, and Flat simulations, respectively.

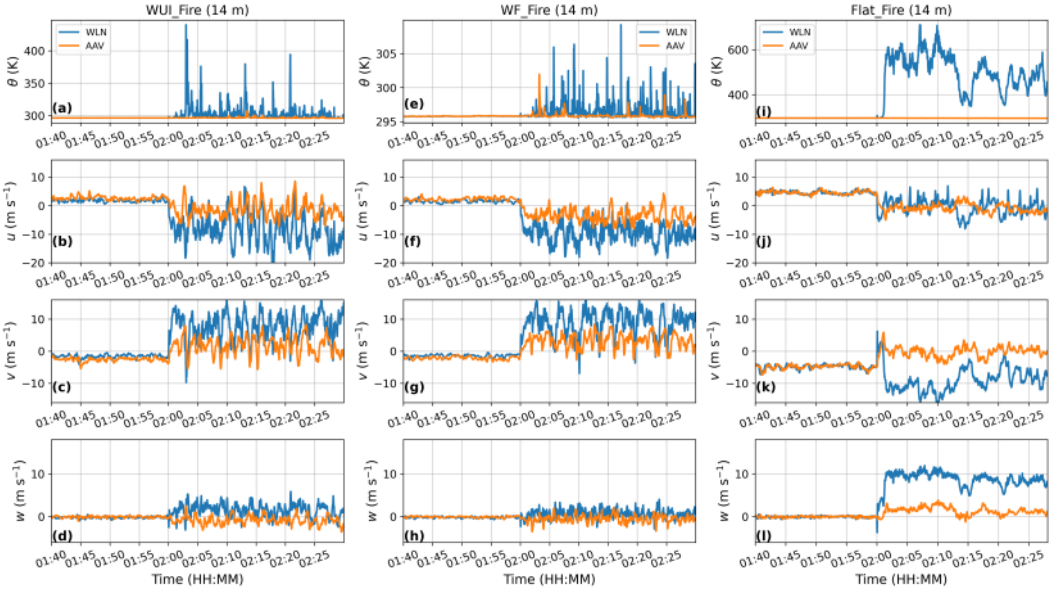

Figure 7. Time series of θ, u, v, and w for WLN and AAV at 14 m above the surface. From left to right, the columns are for WUI_Fire, WF_Fire, and Flat_Fire, respectively. Refer to panels (a), (e), and (i) for color legends. The time series are areal means obtained from grid points marked by the dashed (WLN) and solid (AAV) red lines shown in Figure 5.

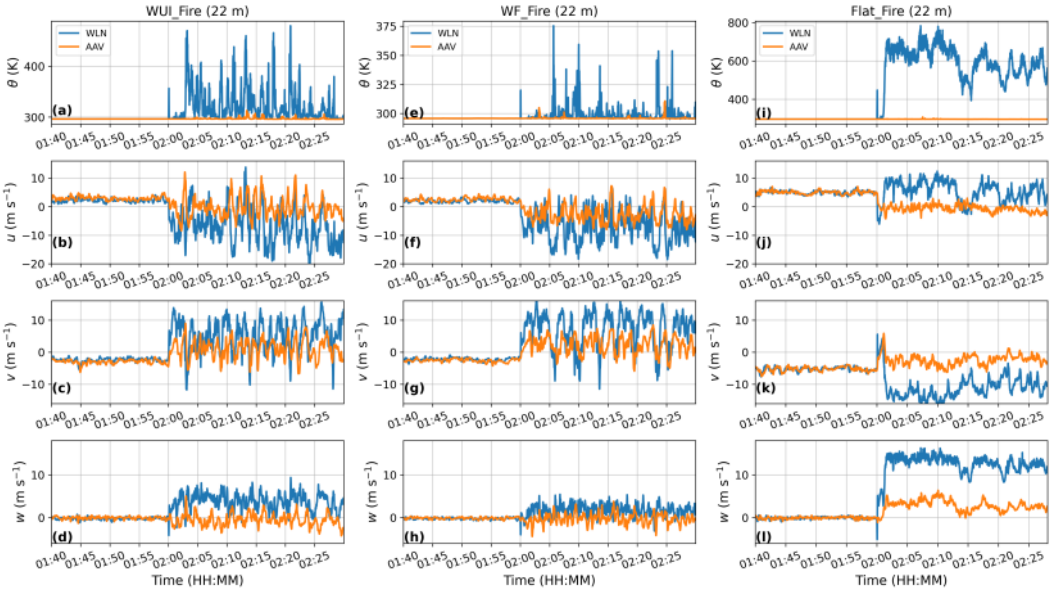

Figure 8. Similar to Figure 7, but for WLN and AAV at 22 m above the surface.

3.4 Temporal evolution of flow variables

To further explore the impact of WUI and the atmospheric flows at the downwind side of the fire, time series of θ and winds at WLN and AAV are presented in Figures 7 and 8. The time series were obtained at two heights: 14 m and 22 m above the surface. Spatial averages were derived for WLN and AAV at the locations marked in Figure 5. Note that in Figure 7i and 8i, the time series of θ for AAV appear to be straight lines due to the scale difference between fire-induced temperature and the ambient atmosphere temperature. This occurs because, in Flat_Fire, the downwind heat barely reaches AAV (as shown in Figure 5c and 5f). With a much higher concentration of heat transported to WLN, θ is well above 400 K most of the time at 14 m and 22 m (Figure 7i and 8i). In WUI_Fire, however, the heat is more sparsely distributed downwind, leading to a less intense increase in temperature (below 450 K at 14 m). The heat pulsing can be identified in Figures 7 and 8 that the temperature increase in WUI_Fire and WF_Fire coincides with short-lived spikes, while the increase in Flat_Fire is long-lasting and more steady. As WLN is closer to the fire than AAV, it shows a stronger impact from the fire in all simulations. Without the urban interface, WF_Fire presents a cooler environment. Although the heat pulsing can be observed in WF_Fire (Figures 7e and 8e), the magnitude of increase in θ is reduced. This suggests that the urban structures promote stronger vertical mixing between the surface and the heat plume, leading to extended downwind heat transport near the surface.

Before the fire is switched on, the magnitudes of winds in WUI_Fire and WF_Fire are smaller than those in Flat_Fire due to a higher surface roughness associated with the WUI and WF. After the fire is switched on, the changes in winds in WUI_Fire and WF_Fire differ considerably from those in Flat_Fire at both heights. Near the mid forest canopy, both WLN and AAV in WUI_Fire and WF_Fire have a strong shift to negative in u (easterly; Figure 7b, f), whereas this negative shift in u is weaker in Flat_Fire (Figure 7j). Regarding v, in WUI_Fire and WF_Fire, both WLN and AAV show a strong shift to southerlies (positive v; Figure 7c, g), with a greater magnitude at WLN. On the contrary, Flat_Fire shows a strong northerly shift of v at WLN (Figure 7k), with v fluctuating around 0 m s^{-1} for the first 2 minutes after the fire was switched on. w in Flat_Fire rises markedly to over 7 m s^{-1} at WLN after the fire was switched on (Figure 7i). The magnitude of such a rise is weaker at AAV with a magnitude of about 3 m s^{-1} at maximum. The increase in w in WUI_Fire and WF_Fire is less steep (Figure 7d, h), while the time series show noticeable periods of negative w at WLN and AAV. Interestingly, after the fire is switched on, the magnitude of w in WUI_Fire is stronger than that in WF_Fire, especially at WLN. This again suggests that the urban interface is responsible for vertical entrainment of the heat plume to the surface.

The time series near the forest canopy height (Figure 8) generally show a similar pattern compared to their 14 m counterparts. In general, the magnitude of changes in all variables is amplified. At AAV, the mean flows of u and v centers around 0 m s^{-1} in WUI_Fire and WF_Fire (Figures 7b-c, 7 f-g, and 8b-c, 8 f-g,). In Flat_Fire, u turns to strong westerly at WLN (Figure 8j), which is opposite to the same u at 14 m (Figure 7j). In WUI_Fire and WF_Fire, the positive maxima of v at WLN are comparable at 14 m and 22 m, while v ramps down from positive (southerly) to negative (northerly) more markedly at the canopy top (Figure 8c, g). However, the time series of v in Flat_Fire only show a slight northerly displacement at 22 m (Figure 8k) compared to those at 14 m (Figure 7k). Moving further from the surface, the vertical motion gets stronger. At the forest canopy height, the upward motion intensifies at WLN in all simulations (Figure 8d, h, l). This amplification is visible but weaker in WF_Fire (Figure 8h). The amplification of vertical motion with height is limited to positive w for AAV in Flat_Fire, in contrast to WF_Fire and WUI_Fire, indicating a weaker downwind fire impact on the flows due to the absence of urban structures and forest canopy. In general, the fire-induced flows in both WUI_Fire and WF_Fire present a more significant transition against the ambient atmospheric flow (northwesterly) than their Flat_Fire counterparts. Additionally, this transition is stronger

in WUI_Fire than in WF_Fire. This agrees with our argument that the WUI substantially modifies the atmospheric flows near the fire.

3.5 Zero-crossing analysis

To quantify heat pulsing in the simulations, the zero-crossing method was applied to the θ time series during the 30-minute fire period. We first obtained the pulsing signal by subtracting the 5-minute rolling mean from the original time series. With the pulsing behavior, the signal crosses its 5-minute rolling mean over time. By counting the number of crossing times and the duration between each crossing, the pulsing frequency can be estimated. The 5-minute interval was chosen for separating turbulent fluctuations from the evolution of the mean flow, based on the wavelet analysis described below (Section 3.6).

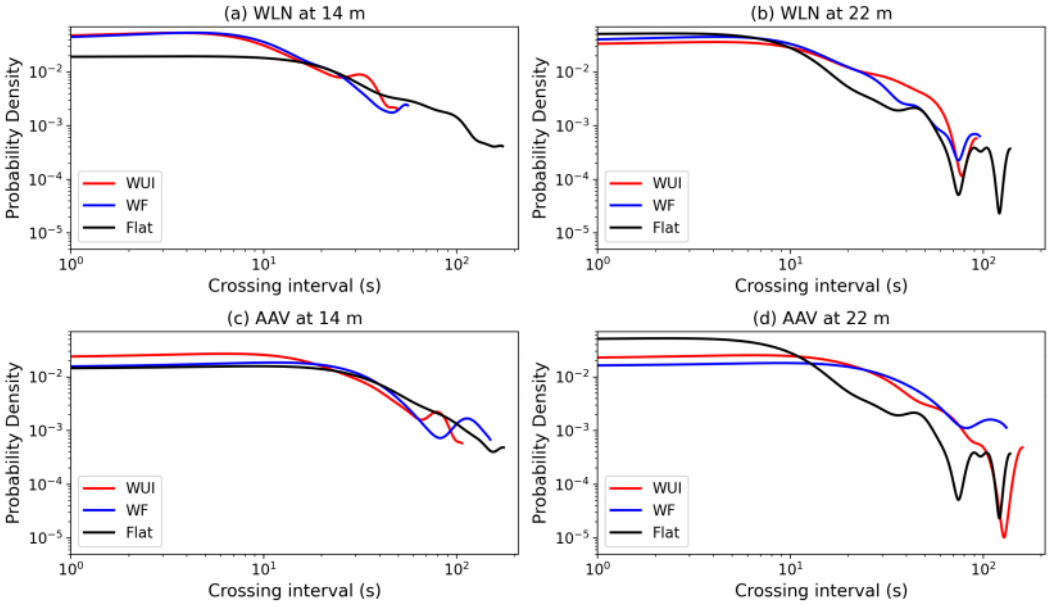

Figure 9. Probability density function (PDF) of zero-crossing periods derived from the time series of θ shown in Figures 7 and 8. The top panels (a-b) show results for the near-fire (WLN) location, and the bottom panels (c-d) show results for the downwind (AAV) location. The left (a, c) and right (b, d) columns are for θ at 14 m and 22 m, respectively. For all panels, both axes are plotted on logarithmic scales to emphasize differences across a range of crossing periods.

Figure 9 shows the probability density functions (PDFs) of zero-crossing intervals for θ at WLN and AAV using the time series shown in Section 3.4. Across all panels, Flat_Fire exhibits a contrasting profile compared to WF_Fire and WUI_Fire. At both 14 m and 22 m, Flat_Fire shows a largely monotonic decrease in the densities with increasing crossing interval, whereas WF_Fire and WUI_Fire display a secondary peak whose size and position change with height. In Flat_Fire, moving from 14 m to 22 m generally results in increased densities at crossing intervals <10 s, reflecting stronger buoyancy-driven fluctuations aloft. This increase in densities with height is absent in WF_Fire and WUI_Fire, suggesting that the presence of forest canopy and urban surfaces modulates fire-induced flow variability.

At WLN near mid forest canopy (14 m; Figure 9a), WF_Fire and WUI_Fire maintain higher densities below 20 s than Flat_Fire, indicating more frequent and sustained pulsing near the fire in the presence of surface heterogeneity. Additionally, WUI_Fire exhibits a secondary peak near 35-40 s, which is weaker in WF_Fire (50-60 s) and absent in Flat_Fire,

suggesting that the urban interface supports intermittent longer-period fluctuations alongside short-period pulsing. Only Flat_Fire shows a long, low-amplitude tail beyond 60–100 s, which likely results from small fluctuations rather than organized heat pulses.

At AAV at 14 m (Figure 9c), peak crossing densities decrease across all cases, consistent with weakening fire influence downstream. This weakening is also reflected in the WF_Fire and WUI_Fire PDFs, where the second peaks shift to longer crossing intervals compared to their WLN counterparts. WUI_Fire also sustains the highest density below 10 s, suggesting that short-period pulses persist farther in the urban interface case.

Moving to the forest canopy top at WLN (22 m; Figure 9b), all simulations show a sharp drop in densities near 70 s and an increase shortly after. Flat_Fire shows the fastest drop-off and the lowest densities at crossing intervals >10 s, suggesting brief, rapid fluctuations without longer-period variability. In contrast, WF_Fire maintains elevated density in the 20–30 s range, while WUI_Fire has the broadest distribution, extending up to ∼60 s. This reflects a wider range of organized fluctuations in more complex surface environments.

At AAV at 22 m (Figure 9d), the PDF of Flat_Fire is similar to that at WLN (Figure 9b), unexpectedly showing the highest density between 10-20 s. Inspection of the time series (not shown) reveals that this results from low-amplitude, high-frequency fluctuations that cross the rolling mean frequently without representing meaningful pulsing. These fluctuations likely reflect undisturbed, weak thermal variability in the absence of canopy or buildings. In contrast, WF_Fire and WUI_Fire maintain higher density above 20 s, consistent with intermittent, longer-period pulses transported downwind through forest canopy-driven or urban-modulated flows. Above 100 s, both WUI_Fire and Flat_Fire show a drop in densities that is absent in WF_Fire, further suggesting that the inclusion of an urban canopy alters the downstream flow.

3.6 Wavelet analysis

To further investigate the temporal characteristics of fire-induced flows and show the differences in the flow dynamics in a more quantitative way, we apply wavelet analysis to θ and w time series at the midpoint grid cell of WLN and AAV. Wavelet transforms allow for examination of frequency variability across time, making them suited for boundary layer turbulence simulation analysis. The resulting power spectra reveal when and at what period dominant fluctuations occur. We focus on θ and w as they most directly represent thermal transport and vertical motion. Figures 10 and 11 show the wavelet power spectra of θ and w, respectively.

Overall, the pulsing behavior is represented by elongated streaks or "fingers" of enhanced power in the θ spectra, extending up to ∼100 s. Note that although we have detrended the time series before wavelet analysis, the fire-induced temperature perturbation is magnitudes higher than the ambient and could overshadow the dynamical features of the ambient atmosphere. Therefore, the high-power fingers are noticeable in the θ spectra, but not in the w spectra. These fingers reflect recurrent, organized bursts of thermal variability. They are most prominent in WUI_Fire and WF_Fire, particularly at WLN (Figure 10a-b). In contrast, Flat_Fire displays weaker and more diffuse power, especially at AAV, suggesting a lack of sustained or coherent pulsing as heat disperses more freely in the absence of surface complexity. The zero-crossing and wavelet analyses capture different aspects of the pulsing behavior. While zero-crossing PDFs reflect how often the signal fluctuates (Figure 9), the wavelet spectra reveal the intensity and duration of fluctuations at different time scales. In WUI_Fire, long-period pulses are less frequent but more energetic, resulting in strong wavelet power at ∼100 s, even though they contribute little to the zero-crossing density at that scale.

In the w spectra, all simulations show consistent short-period variability (4–16 s), but Flat_Fire at AAV exhibits unusually low power even at these scales. This indicates that ver-

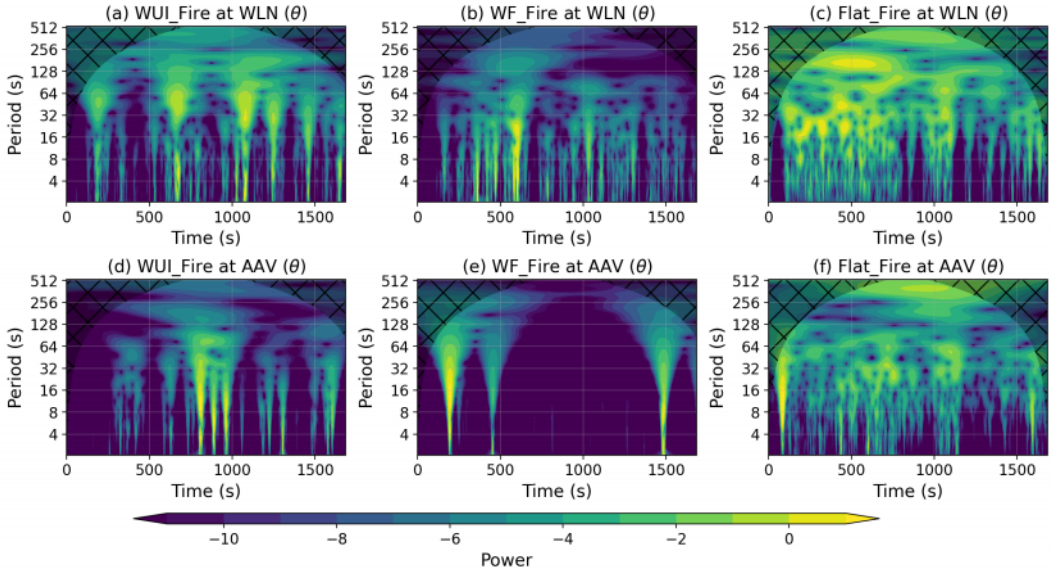

Figure 10. Continuous wavelet power spectra of θ at 22 m above ground level computed using time series extracted from the midpoint grid cell of WLN (top row) and AAV (bottom row) for each simulation. The analysis uses Morlet wavelets, with time on the x-axis and period (s) on the y-axis. Power (log scale) is shown using the color bar, where warmer colors indicate higher energy oscillations at a specific period. The black-hatched region indicates the cone of influence where the distortion of wavelet calculations becomes significant due to insufficient data.

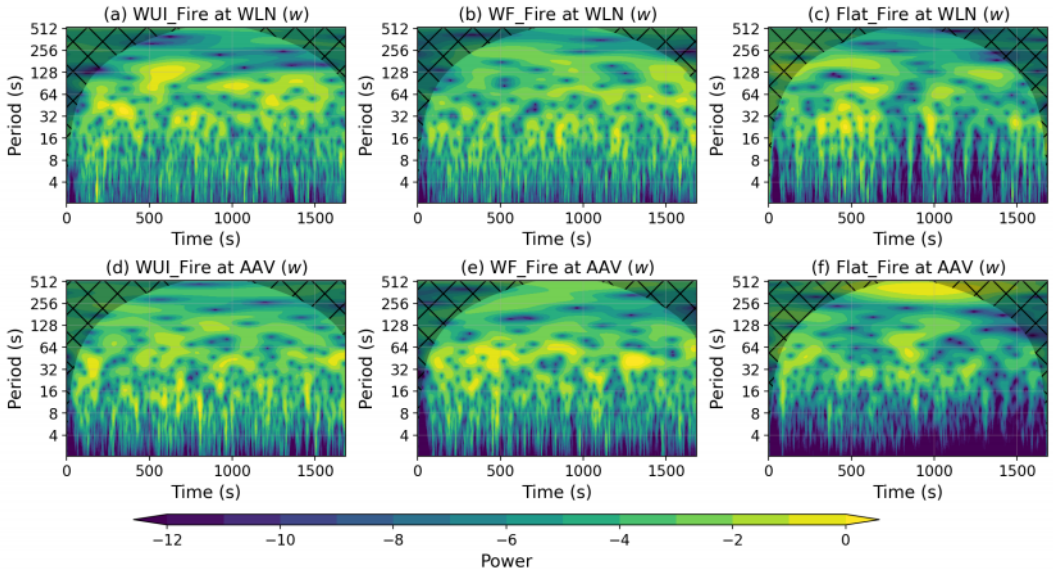

Figure 11. Similar to Figure 10, but for the continuous wavelet power spectra of w at 22 m above the surface.

tical motions weaken significantly with distance in the absence of forest canopy or buildings. Without the mechanical turbulence generated by forest canopy shear or building-induced flow separation, fire-driven buoyant plumes in Flat_Fire rise more freely but exhibit smoother and more continuous vertical motion, with fewer sharp fluctuations. In contrast, the forest canopy and urban buildings in WF_Fire and WUI_Fire introduce entrainment and shear-driven mixing, allowing ambient air to penetrate the plume and generate intermittent vertical accelerations. These interactions sustain vertical variability farther downwind, resulting in stronger short-period (period < 4 s) wavelet power in w.

4 Conclusions and Discussions

This study used high-resolution large-eddy simulations to explore how different landscape types (flat terrain, forested wildland, and WUI) influence atmospheric flow in the presence of a low-intensity fire. Focusing on the BLF WUI, we designed this work as a process-level case study rather than a general-purpose operational model. By prescribing a realistic WUI environment and using turbulence-resolving simulations, we gained new insight into how urban and vegetated structures impact buoyant fire-induced flows.

While our simulations were constrained to a single meteorological scenario and fire configuration, they offer several generalizable insights. Comparison across Flat_Fire, WF_Fire, and WUI_Fire revealed that surface complexity strongly modulates fire-induced fluctuations and subsequently fire heat transport downwind. Specifically, in Flat_Fire, the buoyant plume rises more freely in the absence of surface obstacles, resulting in smoother, more continuous vertical motion and reduced variability both near the surface and downstream. In contrast, the forest canopy and buildings in WF_Fire and WUI_Fire introduced near-surface turbulence, allowing ambient air to interact with the fire heat plume, leading to a transition from buoyancy-dominated to turbulence-modulated regimes.

One intriguing feature observed across all fire simulations was a wave-like structure around 400–600 m in height (Figure S4), consistent with Kelvin–Helmholtz (KH) waves induced by wind shear as shown in Figure 3b-c. Although KH waves produced periodic downdrafts, they were also present in Flat_Fire where heat pulsing was weak or absent, and the downdraft cycles (∼2–3 minutes) did not match the observed pulsing frequencies as shown in zero-crossing (Section 3.5) and wavelet analyses (Section 3.6). Therefore, we conclude that KH waves likely contribute but are not the primary driver of heat pulsing. Instead, downdrafts exiting the forest canopy, as discussed in recent work by Desai et al. (2024), are more likely responsible for generating the observed temperature ramp-cliff structures and pulsed flows. In our simulations, urban structures further modulate the downwind thermal field by extending and dispersing heat pulses through wake interactions and building-induced mixing.

While this study addresses several aspects of WUI fire–atmosphere flows, it is based on a single case study. Ensemble simulations are often required for non-stationary, turbulent systems such as fire-induced atmospheric flows to obtain robust quantities. Recent work by Keskinen and Hellsten (2025) demonstrated that relying solely on time averaging, rather than ensemble averaging, can substantially reduce the accuracy of both the mean and variance in urban LES. However, ensemble LES studies in urban environments remain rare due to the immense computational cost. Keskinen and Hellsten (2025) suggest that 10–50 ensemble members are needed to balance accuracy and cost. A simulation of one hour presented here takes a wall clock time of 24 hours to finish on 900 Intel Skylake CPUs (running at 2.4 GHz) distributed on the Cray XC50 platform. Given such a high computational demand, conducting ensemble simulations is currently infeasible for us. Nonetheless, our case study provides valuable insights into key flow features and dynamics that can inform the design of future ensemble or idealized sensitivity simulations.

Although the current simulations reveal the impacts of wildland forest and WUI on fire-induced flows, our analyses are limited to point-based wavelet and zero-crossing statistics. These represent an initial attempt to disentangle the flow characteristics across different surface configurations (WUI, WF, and Flat), with pulsing behavior emerging as an important avenue for future study. Much remains to be explored in these high-fidelity simulations. Advanced approaches, such as detailed zero-crossing analyses on turbulent flow integral length scale (e.g., Mora & Obligado, 2020), cross-wavelet coherence (e.g., Desai et al., 2024), structure-function methods (e.g., Gibbs & Fedorovich, 2020), and Lagrangian coherent structure techniques (e.g., Aksamit et al., 2024), offer promising ways to identify coherent features and quantify scale-dependent dynamics.

The landscape sensitivity revealed here, where canopy and urban geometry modify plume structure and heat transport, motivates systematic exploration of variables such as building density, street orientation, vegetation type, interface width, and fire intensity. Idealized or semi-idealized simulations guided by these findings can help isolate the influence of individual components, while advanced spectral analyses (e.g., Kiladis et al., 2009; Katurji et al., 2022) may further characterize pulses, entrainment structures, and energy pathways. Finally, future work will extend beyond the prescribed low-intensity forcing used here by coupling PALM with the Wildland–Urban Interface Fire Dynamics Simulator (WFDS Mell et al., 2007) to incorporate fire spread, combustion, and feedback on fire behavior and atmospheric turbulence under more realistic and diverse conditions.

Open Research

We used the 22.10 release of the PALM model available from `https://gitlab.palm-model.org/releases/palm_model_system/-/releases/v22.10` (last accessed: 14 July 2025). The modified version of PALM, all PALM input files for the simulations presented in this study, and data that were used to produce results shown in this study are provided online by Lin (2025). The scientific color maps used in this paper were introduced by Crameri et al. (2020). The Python wrapper can be found at `https://github.com/callumrollo/cmcrameri/tree/main` (last accessed: 14 July 2025). New Zealand WRF and AWS data are freely available on the New Zealand Modeling Consortium at `envlib.org` (last accessed: 14 July 2025)

Disclosure

We have used generative AI tools (ChatGPT and Copilot) only for language polishing and grammar refinement during the manuscript preparation process. All AI-generated content has been reviewed and edited, and we take full responsibility for the final content of this publication.

Acknowledgments

This study was funded by the New Zealand Ministry of Business, Innovation and Employment (MBIE) project "Extreme wildfire: Our new reality – are we ready?" (Grant No. C04X2103). The New Zealand eScience Infrastructure (NeSI) high-performance computing facilities were used to conduct the simulations described in this paper. Simulation testing routines were done on the University of Canterbury high-performance research computing cluster (RCC) and the School of Earth and Environment (SEE) computing cluster.

References

Aksamit, N., Katurji, M., & Zhang, J. (2024). Understanding coherent turbulence and the roll-cell transition with lagrangian coherent structures and frame-indifferent fluxes. *Journal of Geophysical Research: Atmospheres*, *129*(18), e2024JD041490.

Andela, N., Morton, D. C., Giglio, L., Chen, Y., van der Werf, G. R., Kasibhatla, P. S., ... Randerson, J. T. (2017). A human-driven decline in global burned area. *Science*, *356*(6345), 1356–1362. doi: 10.1126/science.aal4108

Bakhshaii, A., & Johnson, E. (2019). A review of a new generation of wildfire–atmosphere modeling. *Canadian Journal of Forest Research*, *49*(6), 565–574. doi: 10.1139/cjfr-2018-0138

Brody-Heine, S., Zhang, J., Katurji, M., Pearce, H. G., & Kittridge, M. (2023). Wind vector change and fire weather index in new zealand as a modified metric in evaluating fire danger. *International Journal of Wildland Fire*. doi: 10.1071/WF22106

Cantor, P., Arruda, M., Firmo, J., & Branco, F. (2023). Development of a standard firebrand accumulation temperature curve for residential wildfire protection system. *Results in Engineering*, *17*, 100935.

Chen, B., Wu, S., Jin, Y., Song, Y., Wu, C., Venevsky, S., ... Gong, P. (2024). Wildfire risk for global wildland–urban interface areas. *Nature Sustainability*, 1–11. doi: 10.1038/s41893-024-01291-0

Clements, C. B., Zhong, S., Goodrick, S., Li, J., Potter, B. E., Bian, X., ... others (2007). Observing the dynamics of wildland grass fires: Fireflux—a field validation experiment. *Bulletin of the American Meteorological Society*, *88*(9), 1369–1382.

Coen, J. (2013). Modeling wildland fires: A description of the coupled atmosphere-wildland fire environment model (cawfe). *University Corporation for Atmospheric Research, Boulder*. doi: 10.5065/D6K64G2G

Coen, J. L., Cameron, M., Michalakes, J., Patton, E. G., Riggan, P. J., & Yedinak, K. M. (2013). Wrf-fire: Coupled weather–wildland fire modeling with the weather research and forecasting model. *Journal of Applied Meteorology and Climatology*, *52*(1), 16–38. doi: 10.1175/JAMC-D-12-023.1

Crameri, F., Shephard, G. E., & Heron, P. J. (2020). The misuse of colour in science communication. *Nature communications*, *11*(1), 5444.

Dahl, N., Xue, H., Hu, X., & Xue, M. (2015). Coupled fire–atmosphere modeling of wildland fire spread using devs-fire and arps. *Natural Hazards*, *77*(2), 1013–1035. doi: 10.1007/s11069-015-1640-y

Dal-Ri dos Santos, I., & Yaghoobian, N. (2023). Effects of urban boundary layer turbulence on firebrand transport. *Fire Safety Journal*, *135*, 103726. doi: 10.1016/j.firesaf.2022.103726

Deardorff, J. W. (1980). Stratocumulus-capped mixed layers derived from a three-dimensional model. *Boundary-Layer Meteorology*, *18*(4), 495–527. doi: 10.1007/BF00119502

Desai, A., Guilloteau, C., Heilman, W. E., Charney, J. J., Skowronski, N. S., Clark, K. L., ... Banerjee, T. (2024). Investigating fire–atmosphere interaction in a forest canopy using wavelets. *Boundary-Layer Meteorology*, *190*(5), 21.

Dickinson, M. B., Wold, C. E., Butler, B. W., Kremens, R. L., Jimenez, D., Sopko, P., & O'Brien, J. J. (2021). The wildland fire heat budget—using bi-directional probes to measure sensible heat flux and energy in surface fires. *Sensors*, *21*(6), 2135. doi: 10.3390/s21062135

Envirionment Canterbury Regional Council. (2020). *Christchurch and ashley river, canterbury, new zealand 2018.* doi: https://doi.org/10.5069/G91J97WQ

Filippi, J.-B., Pialat, X., & Clements, C. B. (2013). Assessment of forefire/meso-nh for wildland fire/atmosphere coupled simulation of the fireflux experiment. *Proceedings of the Combustion Institute*, *34*(2), 2633–2640. doi: 10.1016/j.proci.2012.07.022

Finney, M. A., Cohen, J. D., Forthofer, J. M., McAllister, S. S., Gollner, M. J., Gorham, D. J., ... English, J. D. (2015). Role of buoyant flame dynamics in wildfire spread. *Proceedings of the National Academy of Sciences*, *112*(32), 9833–9838. doi: 10.1073/pnas.1504498112

Fire Emergency New Zealand. (2021). *New zealand wildfire summary 2020/21 wildfire season update.* Retrieved from `https://www.fireandemergency.nz/assets/Documents/Research-and-reports/NZ-Wildfire-2020-21-Season-update-Scion.pdf` ([On-

line; accessed 2024-06-21])

Fire Emergency New Zealand. (2022). *Lake Ōhau wildfire investigation report and operational review.* Retrieved from `https://www.fireandemergency.nz/research-and-reports/operational-reviews-and-reports/lake-ohau-wildfire-investigation-report-and-operational-review/` ([Online; accessed 2024-06-21])

Gehrke, K. F., Sühring, M., & Maronga, B. (2021). Modeling of land–surface interactions in the palm model system 6.0: land surface model description, first evaluation, and sensitivity to model parameters. *Geoscientific Model Development*, *14*(8), 5307–5329. doi: 10.5194/gmd-14-5307-2021

Gibbs, J. A., & Fedorovich, E. (2020). Structure functions and structure parameters of velocity fluctuations in numerically simulated atmospheric convective boundary layer flows. *Journal of the Atmospheric Sciences*, *77*(10), 3619–3630.

Gutierrez, A. A., Hantson, S., Langenbrunner, B., Chen, B., Jin, Y., Goulden, M. L., & Randerson, J. T. (2021). Wildfire response to changing daily temperature extremes in california's sierra nevada. *Science Advances*, *7*(47), eabe6417. doi: 10.1126/sciadv.abe6417

Heilman, W. E., Clark, K. L., Bian, X., Charney, J. J., Zhong, S., Skowronski, N. S., ... Patterson, M. (2021). Turbulent momentum flux behavior above a fire front in an open-canopied forest. *Atmosphere*, *12*(8), 956.

Heilman, W. E., Clements, C. B., Seto, D., Bian, X., Clark, K. L., Skowronski, N. S., & Hom, J. L. (2015). Observations of fire-induced turbulence regimes during low-intensity wildland fires in forested environments: implications for smoke dispersion. *Atmospheric Science Letters*, *16*(4), 453–460.

Holden, Z. A., Swanson, A., Luce, C. H., Jolly, W. M., Maneta, M., Oyler, J. W., ... Affleck, D. (2018). Decreasing fire season precipitation increased recent western us forest wildfire activity. *Proceedings of the National Academy of Sciences*, *115*(36), E8349–E8357. doi: 10.1073/pnas.1802316115

Katurji, M., Noonan, B., Zhang, J., Valencia, A., Shumacher, B., Kerr, J., ... Zawar-Reza, P. (2022). Atmospheric turbulent structures and fire sweeps during shrub fires and implications for flaming zone behaviour. *International Journal of Wildland Fire*, *32*(1), 43–55. doi: 10.1071/WF22100

Keskinen, J.-P., & Hellsten, A. (2025). Ensembles in urban large eddy simulations with changing wind direction. *Boundary-Layer Meteorology*, *191*(7), 1–36.

Kiefer, M. T., Heilman, W. E., Zhong, S., Charney, J. J., & Bian, X. (2015). Mean and turbulent flow downstream of a low-intensity fire: Influence of canopy and background atmospheric conditions. *Journal of Applied Meteorology and Climatology*, *54*(1), 42–57.

Kiefer, M. T., Heilman, W. E., Zhong, S., Charney, J. J., & Bian, X. (2016). A study of the influence of forest gaps on fire–atmosphere interactions. *Atmospheric Chemistry and Physics*, *16*(13), 8499–8509.

Kiefer, M. T., Zhong, S., Charney, J. J., Bian, X., Heilman, W. E., & Seitz, J. (2024). A numerical study of smoke concentration distribution near low-intensity fires: Sensitivity to vertical canopy structure and fire heat source strength. *Journal of Applied Meteorology and Climatology*.

Kiefer, M. T., Zhong, S., Heilman, W. E., Charney, J. J., & Bian, X. (2018). A numerical study of atmospheric perturbations induced by heat from a wildland fire: Sensitivity to vertical canopy structure and heat source strength. *Journal of Geophysical Research: Atmospheres*, *123*(5), 2555–2572.

Kiladis, G. N., Wheeler, M. C., Haertel, P. T., Straub, K. H., & Roundy, P. E. (2009). Convectively coupled equatorial waves. *Reviews of Geophysics*, *47*(2).

Krč, P., Resler, J., Sühring, M., Schubert, S., Salim, M. H., & Fuka, V. (2021). Radiative transfer model 3.0 integrated into the palm model system 6.0. *Geoscientific Model Development*, *14*(5), 3095–3120. doi: 10.5194/gmd-14-3095-2021

Landcare Research. (2020). *Lcdb v5.0 - land cover database version 5.0, mainland new*

zealand. Retrieved from https://lris.scinfo.org.nz/layer/104400-lcdb-v50-land-cover-database-version-50-mainland-new-zealand/ ([Online; accessed 2020-07-15])

Lin, D. (2025, August). *Data and model resources for bottle lake forest WUI fire simulations using PALM [Collection]*. Zenodo. doi: 10.5281/zenodo.16658836

Lin, D., Katurji, M., Revell, L. E., Khan, B., & Sturman, A. (2023). Investigating multiscale meteorological controls and impact of soil moisture heterogeneity on radiation fog in complex terrain using semi-idealised simulations. *Atmospheric Chemistry and Physics*, *23*(22), 14451–14479. doi: 10.5194/acp-23-14451-2023

Lin, D., Khan, B., Katurji, M., Bird, L., Faria, R., & Revell, L. E. (2021). Wrf4palm v1.0: a mesoscale dynamical driver for the microscale palm model system 6.0. *Geoscientific Model Development*, *14*(5), 2503–2524. doi: 10.5194/gmd-14-2503-2021

Lin, D., Zhang, J., Khan, B., Katurji, M., & Revell, L. E. (2024). Geo4palm v1.1: an open-source geospatial data processing toolkit for the palm model system. *Geoscientific Model Development*, *17*(2), 815–845. doi: 10.5194/gmd-17-815-2024

Linn, R., Reisner, J., Colman, J. J., & Winterkamp, J. (2002). Studying wildfire behavior using firetec. *International Journal of Wildland Fire*, *11*(4), 233. doi: 10.1071/WF02007

Maronga, B., Banzhaf, S., Burmeister, C., Esch, T., Forkel, R., Fröhlich, D., ... Russo, E. (2020). Overview of the palm model system 6.0. *Geoscientific Model Development*, *13*, 1335–1372.

Maronga, B., Gryschka, M., Heinze, R., Hoffmann, F., Kanani-Sühring, F., Keck, M., ... Raasch, S. (2015). The parallelized large-eddy simulation model (palm) version 4.0 for atmospheric and oceanic flows: model formulation, recent developments, and future perspectives. *Geoscientific Model Development*, *8*(8), 2515–2551. doi: 10.5194/gmd-8-2515-2015

Matvienko, O., Kasymov, D., Loboda, E., Lutsenko, A., & Daneyko, O. (2022). Modeling of wood surface ignition by wildland firebrands. *Fire*, *5*(2), 38. doi: 10.3390/fire5020038

Mell, W., Jenkins, M. A., Gould, J., & Cheney, P. (2007). A physics-based approach to modelling grassland fires. *International Journal of Wildland Fire*, *16*(1), 1–22. doi: 10.1071/WF06002

Mora, D. O., & Obligado, M. (2020). Estimating the integral length scale on turbulent flows from the zero crossings of the longitudinal velocity fluctuation. *Experiments in fluids*, *61*(9), 199.

Mueller, S. E., Thode, A. E., Margolis, E. Q., Yocom, L. L., Young, J. D., & Iniguez, J. M. (2020). Climate relationships with increasing wildfire in the southwestern us from 1984 to 2015. *Forest Ecology and Management*, *460*, 117861. doi: 10.1016/j.foreco.2019.117861

Pearce, H. (2018). The 2017 port hills wildfires-a window into new zealand's fire future? *Australasian Journal of Disaster and Trauma Studies*, *22*, 35–50.

Perry, G. L. W., Wilmshurst, J. M., & McGlone, M. S. (2014). Ecology and long-term history of fire in new zealand. *New Zealand Journal of Ecology*, *38*(2), 157–176.

Radeloff, V. C., Hammer, R. B., Stewart, S. I., Fried, J. S., Holcomb, S. S., & McKeefry, J. F. (2005). The wildland-urban interface in the united states. *Ecological Applications*, *15*(3), 799–805.

Resler, J., Krč, P., Belda, M., Juruš, P., Benešová, N., Lopata, J., ... Kanani-Sühring, F. (2017). Palm-usm v1.0: A new urban surface model integrated into the palm large-eddy simulation model. *Geoscientific Model Development*, *10*(10), 3635–3659. doi: 10.5194/gmd-10-3635-2017

Sturman, A. P., & Tapper, N. J. (2006). *The weather and climate of australia and new zealand*. Oxford University Press, USA.

Sullivan, A., Baker, E., Kurvits, T., Popescu, A., Paulson, A. K., Cardinal Christianson, A., ... Robinson, C. (2022). Spreading like wildfire: The rising threat of extraordinary landscape fires.

Sullivan, A. L. (2009a). Wildland surface fire spread modelling, 1990 - 2007. 1: Physical

and quasi-physical models. *International Journal of Wildland Fire*, *18*(4), 349. doi: 10.1071/WF06143

Sullivan, A. L. (2009b). Wildland surface fire spread modelling, 1990 - 2007. 2: Empirical and quasi-empirical models. *International Journal of Wildland Fire*, *18*(4), 369. doi: 10.1071/WF06142

Sullivan, A. L. (2017). Inside the inferno: Fundamental processes of wildland fire behaviour. *Current Forestry Reports*, *3*(2), 150–171. doi: 10.1007/s40725-017-0058-z

Tang, T. (2017). A physics-based approach to modeling wildland fire spread through porous fuel beds. *Theses and Dissertations–Mechanical Engineering*. doi: https://doi.org/10.13023/ETD.2017.027

Tse, S. D., & Fernandez-Pello, A. C. (1998). On the flight paths of metal particles and embers generated by power lines in high winds—a potential source of wildland fires. *Fire Safety Journal*, *30*(4), 333–356. doi: 10.1016/S0379-7112(97)00050-7

Valencia, A., Melnik, K. O., Kelly, R. J., Jerram, T. C., Wallace, H., Aguilar-Arguello, S., ... Strand, T. (2023). Mapping fireline intensity and flame height of prescribed gorse wildland fires. *Fire Safety Journal*, *140*, 103862. doi: 10.1016/j.firesaf.2023.103862

Valencia, A., Melnik, K. O., Sanders, N., Hoy, A. S., Yan, M., Katurji, M., ... Strand, T. (2023). Influence of fuel structure on gorse fire behaviour. *International Journal of Wildland Fire*, *32*(6), 927–941. doi: 10.1071/WF22108

Zhang, J., Katurji, M., Zawar-Reza, P., & Strand, T. (2023). The role of helicity and fire–atmosphere turbulent energy transport in potential wildfire behaviour. *International Journal of Wildland Fire*, *32*(1), 29–42. doi: 10.1071/WF22101